Parameter Estimation for Single-Dipole Experiments

Jordan Mirocha[1,2,*], Geraint J.A. Harker[3], Jack O. Burns[1,4], Jonathan R. Pritchard[5]

[1]University of Colorado, [2]UCLA, [3]University College London, [4]NASA Ames Research Center, [5]Imperial College London

*Contact Email: mirocha@astro.ucla.edu

Introduction

We investigate two important issues in the extraction and interpretation of the global 21-cm signal. First, we introduce a new parameterization of the global 21-cm signal that provides a computationally inexpensive substitute for more sophisticated physical models but is still flexible enough to match the shape of physical models rather well. We explore its utility in an idealized signal extraction exercise in which the signal and foreground are fit simultaneously using a Markov Chain Monte Carlo approach. Second, with the constraints on the global 21-cm extrema ("turning points") from this procedure, we subsequently fit a more computationally expensive, but physically-motivated, model, which relates the production rate of Lyman-α, Lyman continuum, and X-ray photons to the rate at which gas collapses onto dark matter halos exceeding some minimum virial temperature, T_{min}. Our results are summarized briefly here, and in more detail in two upcoming papers (Harker et al. (2015), submitted to MNRAS, Mirocha et al. (2015), accepted for publication in ApJ).

Part I. Signal Extraction

We follow the Markov Chain Monte Carlo (MCMC) approach of Harker et al. (2012) with a few important modifications. Most notably, rather than modeling the global 21-cm signal as a spline fit to the "turning points" of the signal, we use a more physically-motivated model which treats the evolution of the background Lyman-α intensity, $J_\alpha(z)$, thermal history, $T_k(z)$ and ionization history, $x_i(z)$, as independent $tanh$ functions, i.e.,

$$A(z) = \frac{A_{ref}}{2}\left\{1 + \tanh\left[\frac{z_0 - z}{\Delta z}\right]\right\}$$

where A_{ref} normalizes each quantity, z_0 is the redshift at which each quantity "turns on," and Δz is the redshift interval over which each quantity evolves from negligible values to a saturated limit. This model matches the shape of physical models much better than the spline approach, and because it is related to physical quantities, also can more easily constrain the overall normalization of the signal (see Figure 1 below), e.g., because physical histories require $A_{ref}=1$ for the ionization history.
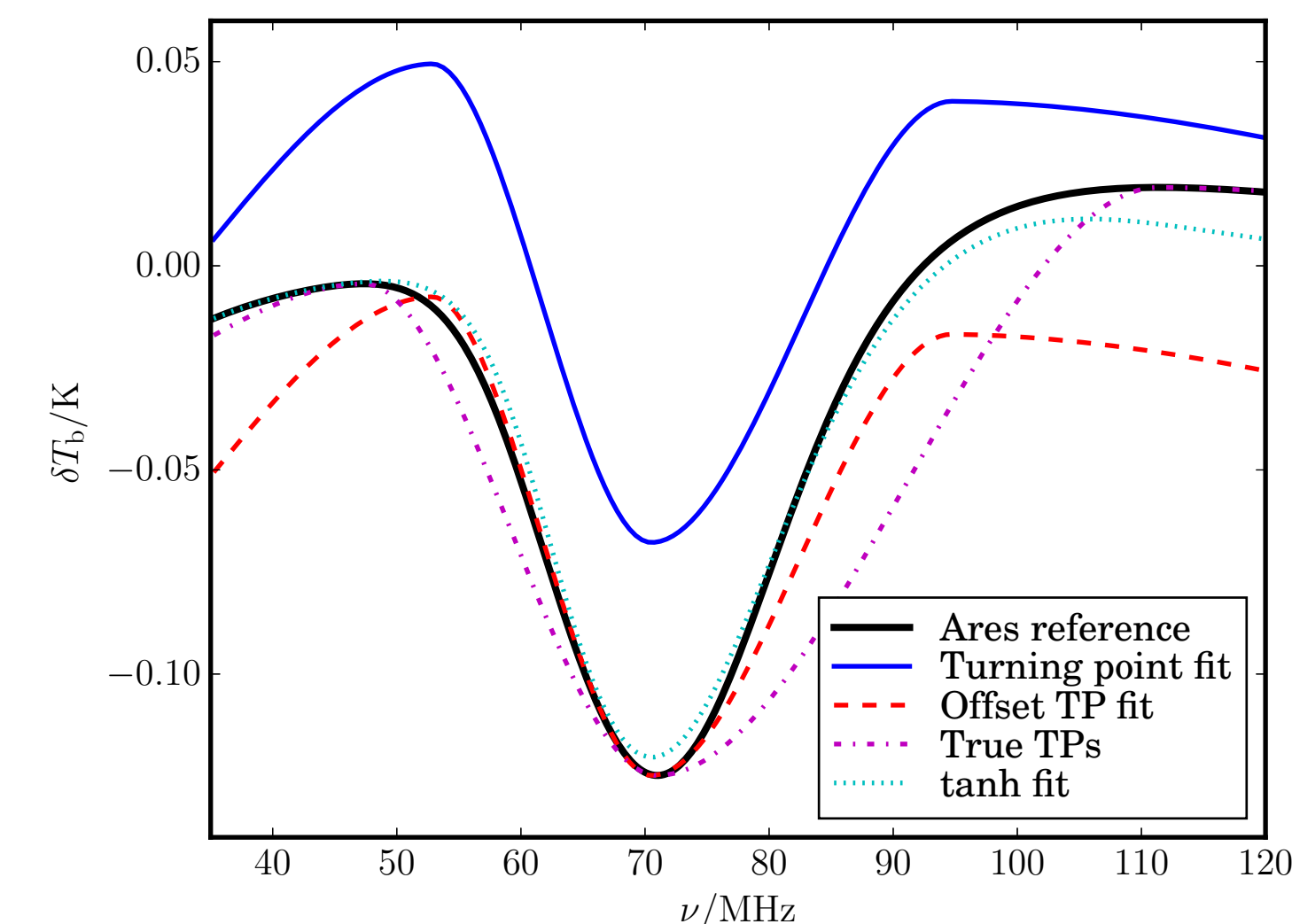
Figure 1: Comparison of best-fit reconstructed tanh model (dotted cyan) compared to previous spline approach (solid blue). The input model, computed with the ARES code, is shown in solid black, and is identical to the solid black curve in each panel of Figure 3. The dashed red curve shows the best-fit spline model shifted downward such that it matches the absorption minimum of the input signal. The "true" spline representation of the input model is shown by the dashed magenta curve.

With the $tanh$ model, increasing the integration time has a larger effect than increasing the number of independent sky regions observed (see Figure 2 below). This is because of its relation to physical quantities, which have well-understood bounds (e.g., $x_i=1$ at the end of reionization, the IGM temperature cannot fall below the limit set by the Hubble expansion, etc.). For very precise measurements, however, the recovered positions of the turning points can be biased (see 1000 hr results in Figure 2). This is driven by degeneracies between the signal and foreground at high frequencies ($\nu > 100$ MHz), which can be mitigated by higher order foreground models. See Harker et al. (2015) for more discussion of this result.
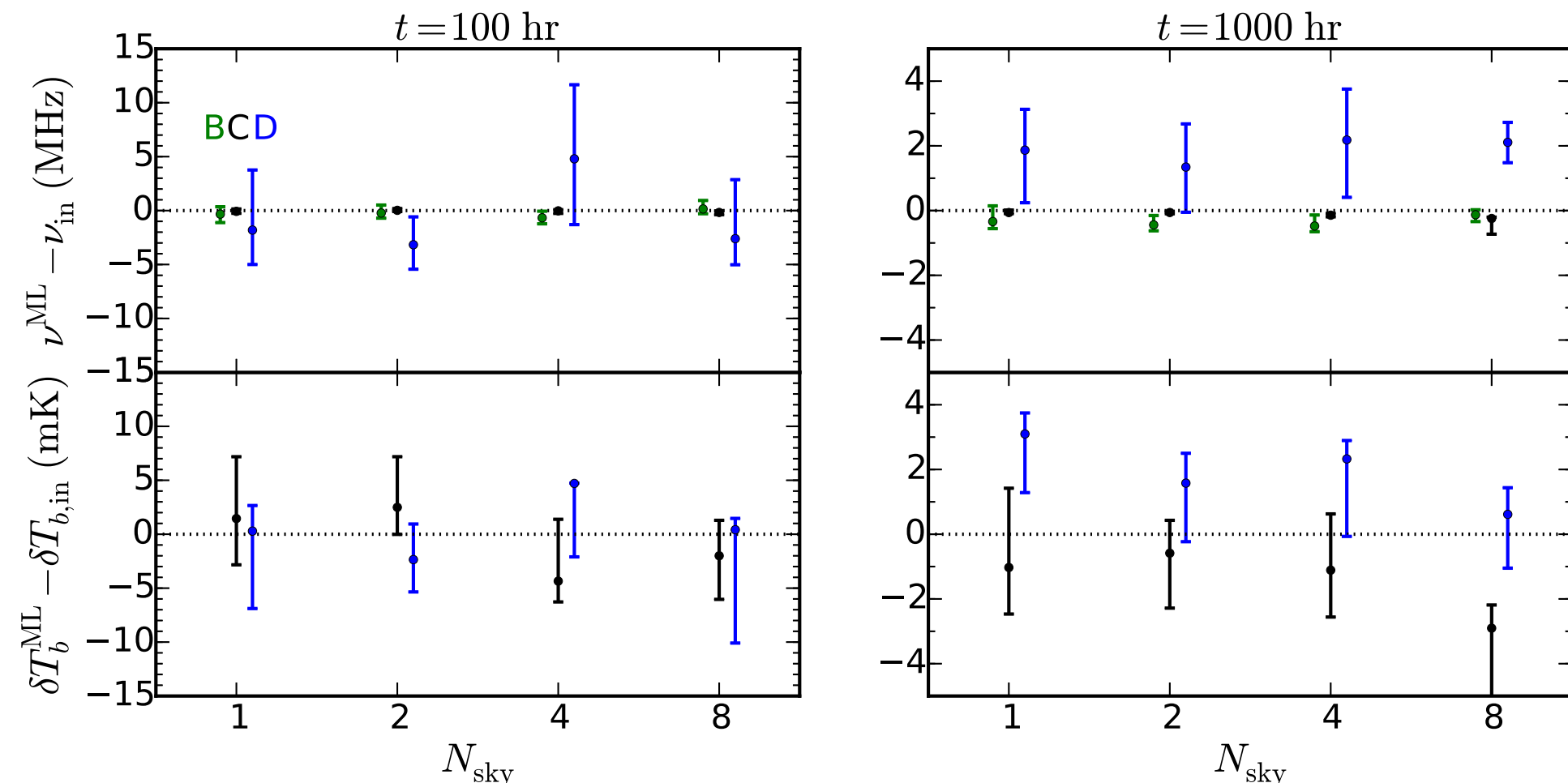
Figure 2: Trade-off between number of independent sky regions observed, N_{sky}, and total integration time, t_{int}, as evidenced by the recovered positions of turning points B, C, D (annotated in Figures 1 and 3). The top row shows the recovered position in frequency, relative to the maximum-likelihood value, for each of the turning points, while the bottom row is the analogous quantity for the amplitude of each feature. Note the difference in the scale of the y-axis between the left and right columns.

Part II. Constraints on the Physical Model and the IGM

For the results that follow, we focus only on the 100 hour constraints for 1 and 2 sky regions presented in the previous section. Treating the constraints on the turning points as independent Gaussians, we proceed to fit a physical model, similar to those presented in the literature in recent years (e.g., Furlanetto 2006). The star-formation history is related to the rate at which gas collapses into dark matter halos, i.e.,

$$\dot{\rho}_*(z) \propto f_* \frac{df_{coll}}{dt}$$

where $f_{coll}=f_{coll}(T_{min})$, and f_* is the star formation efficiency. Three additional parameters are required to convert star formation into Ly-α, Ly-C (i.e., ionizing photons), and X-ray photons, which we represent with the parameter ξ (see Figure 3). The star formation efficiency is absorbed into each ξ parameter.

From this fit, we obtain constraints on the parameters of the model (see Fig. 4 below), in addition to the properties of the IGM as a function of time (Figures 6 and 7 at right). Figures 4,6, and 7 all show the results of two calculations: the first assuming a single pointing for 100 hours (open contours), and the second assuming 100 hours split between two independent sky regions (filled contours). The latter also assumes a more complex foreground model, which improves constraints at high frequencies and thus primarily constraints on ξ_ion (Fig. 4) and the ionization history (Fig. 7)

Figure 3: Basic dependencies of the global 21-cm signal. The black line is the same in each panel, representing our reference model, while all solid green (blue) lines correspond to a factor of 2 increase (decrease) in the parameter noted in the upper left corner, and dashed lines are factor of 10 changes above and below the reference value. The dotted lines show the maximum allowed amplitude of the signal (i.e., the amplitude of the signal when $x_i = 0$ and $T_S \gg T_{CMB}$), and the minimum allowed amplitude of the signal (set by assuming $T_S = T_k = T_{ad}$, where T_{ad} is the gas temperature in an adiabatically-cooling Universe). Turning points B, C, and D are annotated in the lower left panel for reference.

Figure 5: Relationship between parameters ξ_LW and ξ_ion (panel e in Figure 4) and the properties of a stellar population. The cross-hatched band corresponds to the ratio ξ_LW/ξ_ion for a pure 50,000 K blackbody, while the blue and red bands correspond to ξ_LW/ξ_ion values for Salpeter and bottom-heavy stellar initial mass functions (IMF), respectively, as computed with starburst99. The width of each band corresponds to a factor of 2 change in the escape fraction of ionizing radiation, between 10% and 20%.
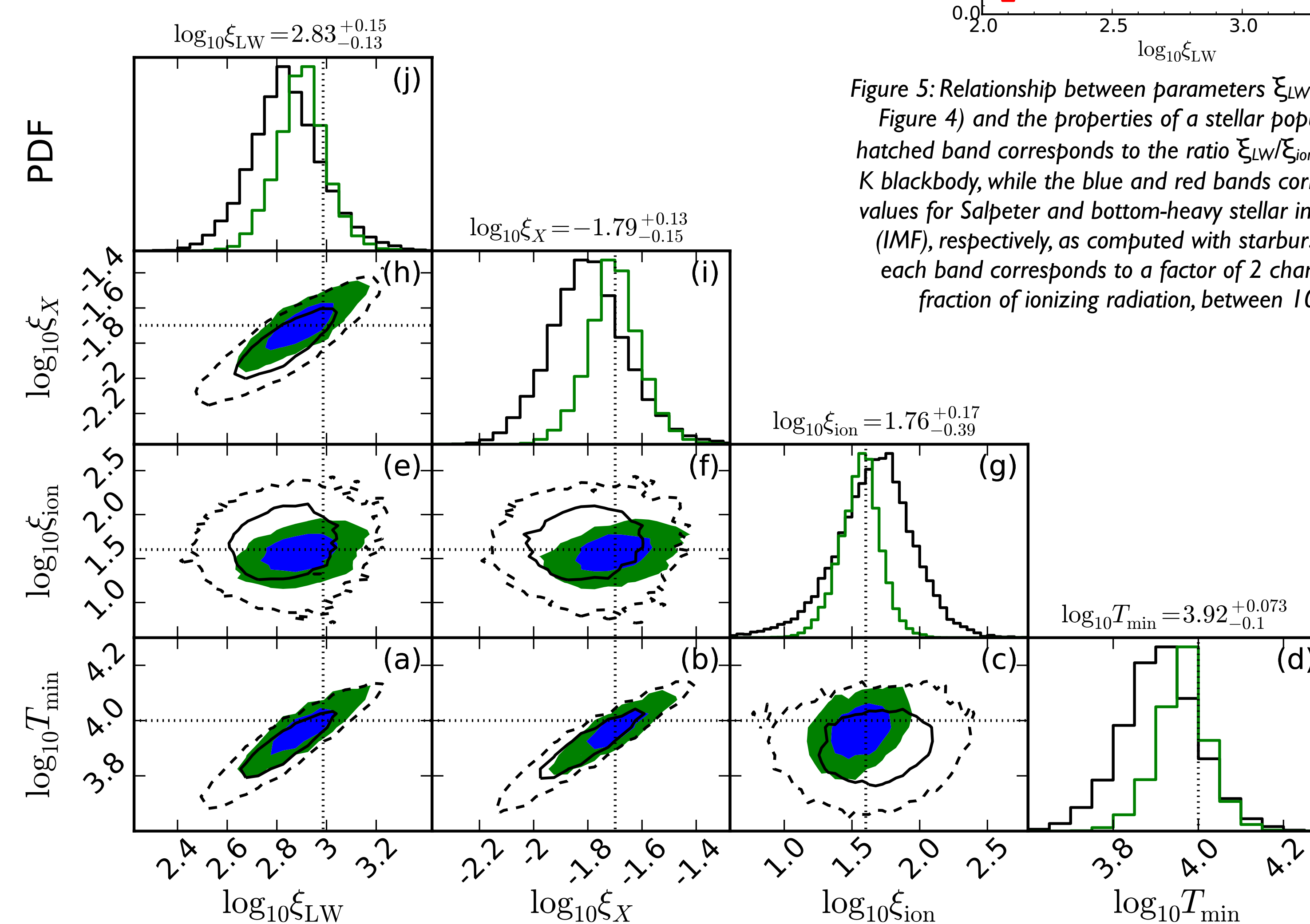
Figure 4: Constraints on our 4-parameter reference model. Filled contours in the interior panels are 2-D marginalized posterior PDFs with 68% confidence intervals shaded blue and 95% confidence regions in green. Panels along the diagonal are 1-D marginalized posterior PDFs for each input parameter, with 1-σ asymmetric error-bars corresponding to the green histograms. Dotted lines denote the input values of our reference model (solid black lines, Figure 1 & 3). Annotated best-fit values and error bars along the diagonal are those associated with the filled contours, in which the 100 hours of observation were split between 2 sky regions, and the foreground was treated as a 4th order polynomial, rather than 3rd. Panel (e) is investigated in more detail above the diagonal in Figure 5.

Conclusions & Ongoing Work

Our calculations suggest that somewhat modest observations (one or two sky regions and 100 hours of integration) can constrain physical models quite well, to ~0.1 dex (68% confidence) in each dimension (see Figure 4). Constraints on the physical model are accompanied by constraints on the IGM (Figures 6 & 7), most notably providing strong evidence for the beginning of reionization (panel j in Figure 7), so long as turning point D is detected with confidence. It is advantageous to observe multiple sky regions, though the improvement beyond 2 sky regions is modest (see Figure 2). Our calculations assumed (i) that all three spectral turning points fell within the 40-120 MHz band, (ii) an idealized instrument with a flat response and a Gaussian beam, and (iii) model parameters that do not vary with redshift. We are currently working on extending these techniques to more realistic scenarios, including treatment of the response function and beam pattern of the Dark Ages Radio explorer (Burns et al. 2015, in prep.), and more complex physical models including feedback.
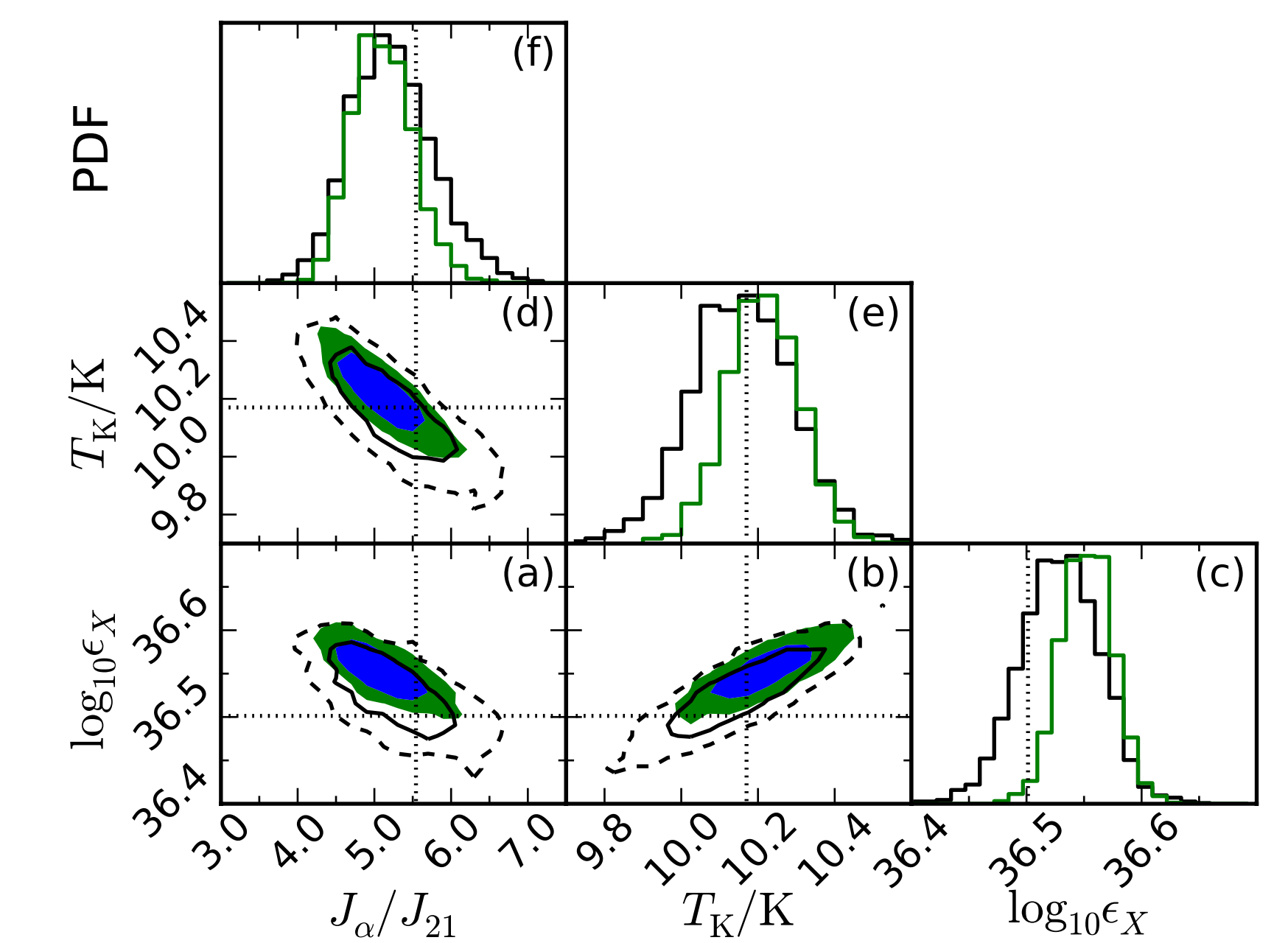
Figure 6: Constraints on (from left to right along the bottom) the Ly-α background intensity, IGM temperature, and heating rate density at the redshift of turning point C. The heating rate density, ϵ_X, is expressed in units of erg / s / cMpc³, while $J_\alpha(z)$ is expressed in units of $J_{21}=10^{-21}$ erg / s / cm² / Hz / sr. Dotted vertical lines show the input values, which occur at z=19 in the reference model. Open contours are 68% (solid) and 95% (dashed) confidence regions for the single sky region fit, while filled contours show the results of the multiple sky region fit, with 68% and 95% confidence regions shown in blue and green, respectively.
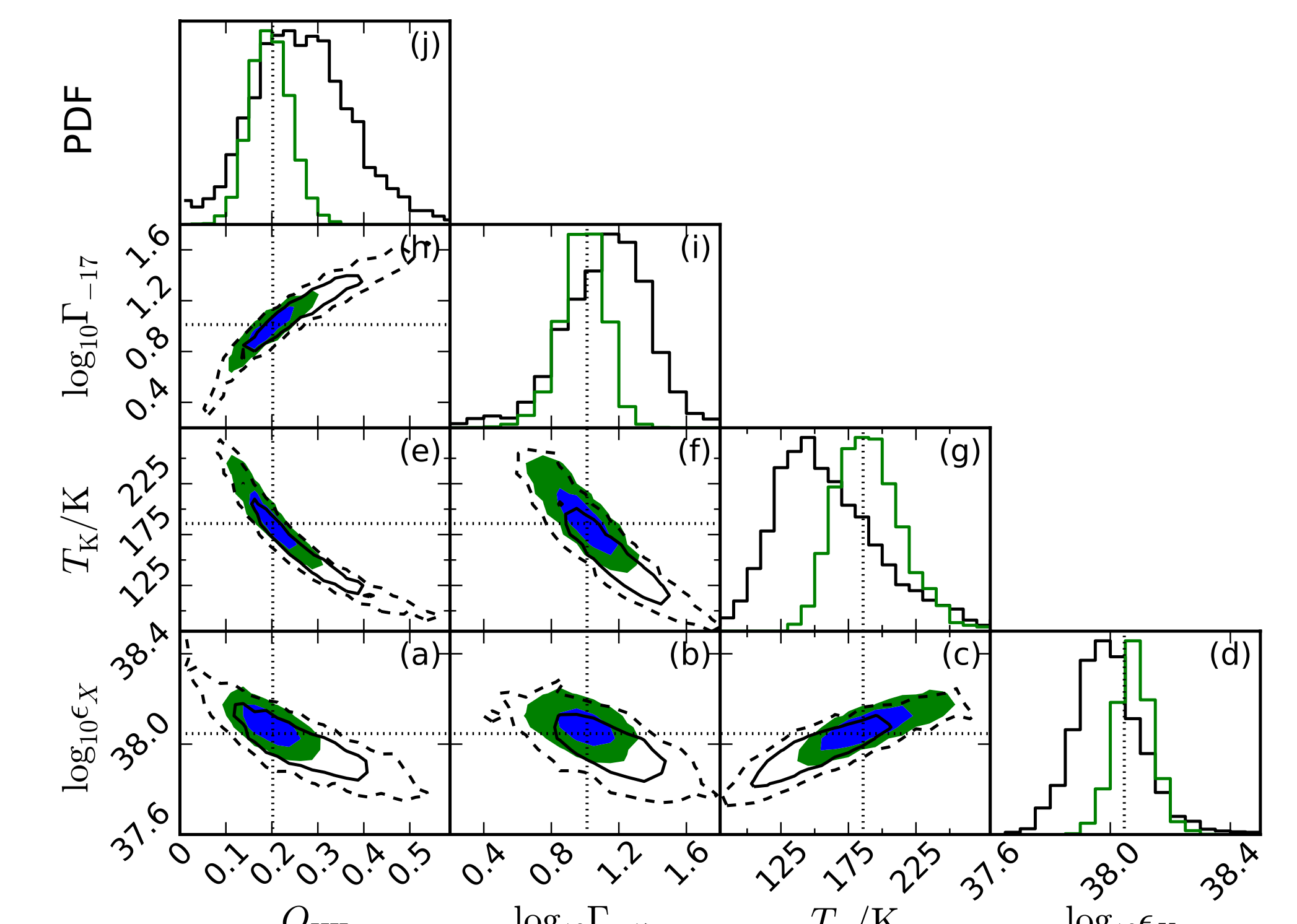
Figure 7: Constraints on (from left to right along the bottom) the volume-filling factor of ionized gas, volume-averaged ionization rate, IGM temperature, and heating rate density at the redshift of turning point D, which occurs at z=11.75 in our reference model. Input values are denoted by black dotted lines in each panel. Color and linestyle conventions are the same as those in Figures 4 and 6.

Acknowledgements

References

Burns et al., 2015, in prep.

Furlanetto, S. R. 2006, MNRAS, 371, 867

Harker, G. J. A., Pritchard, J. R., Burns, J. O., & Bowman, J. D. 2012, MNRAS, 419, 1070

Harker, Mirocha, Burns, Pritchard, submitted to MNRAS

Mirocha, Harker, Burns, accepted for publication in ApJ (arXiv: 1509.07868)